

Ability of exponential data consistency conditions to detect motion in SPECT despite other physical effects

Antoine Robert¹, David Sarrut^{1,2}, Ane Etxebeste¹, Jean Michel Létang¹, and Simon Rit¹

¹Univ.Lyon, INSA-Lyon, Université Claude Bernard Lyon 1, UJM-Saint Etienne, CNRS, Inserm, CREATIS UMR 5220, U1206, F-69373, Lyon, France.

²Centre Léon Bérard, 28, rue Laennec, 69373 Lyon Cedex 08, France

Abstract Exponential data consistency conditions (eDCCs) are equations that express the redundancy of information between exponential projections. Exponential projections can be derived from parallel SPECT projections and be used to detect and correct for patient motion during the acquisition. However, other physical effects such as collimator resolution, scatter or noise could also introduce inconsistencies in the projections. The purpose of this work was to evaluate the impact of these effects on the eDCCs. We used ray-tracing and Monte Carlo simulations to generate different sets of projections and compared their consistency with two metrics based on eDCCs: the absolute relative difference and a noise-aware metric that takes into account the acquisition noise. The collimator resolution, the scatter and the movement increase significantly the error in the eDCCs. The noise-aware metric was more sensitive to patient motion than other effects.

1 Introduction

Single photon emission computed tomography (SPECT) is a key tool for diagnostic imaging which is also used for treatment planning and monitoring of radionuclide therapies. The long acquisition time makes SPECT imaging subject to blur and artifacts due to patient motion. This motion also induces a mismatch between the emission and attenuation maps that may impact the quality of the SPECT images [1].

Data consistency conditions (DCCs) are equations that express the redundancy of information between projections. DCCs have been used in PET to correct for patient motion and to align the emission and attenuation maps [2]. In SPECT, DCCs have also been used to estimate the attenuation map from the emission projections [3]. More recently, Wells *et al* [4] used exponential data consistency conditions (eDCCs) to align the attenuation map to cardiac SPECT data after rebinning pinhole data to parallel projections. eDCCs are less restrictive than SPECT DCCs in that they do not require projections taken over 360°. Wells *et al* [4] used simulated projections to evaluate eDCCs but they did not take into account the scatter or the collimator resolution, which we refer to as the point spread function (PSF) in the following. Moreover, in parallel SPECT systems, projections are acquired sequentially and may be affected by patient motion.

The purpose of this work was to assess the impact of physical effects and motion on the eDCCs. To that end, ray tracing and Monte Carlo simulations were used to generate several sets of projections and to evaluate two metrics based on eDCCs.

2 Materials and Methods

2.1 Exponential data consistency condition

In parallel SPECT, measurements can be modeled by the attenuated Radon transform. Let $f(\vec{x})$, $\vec{x} \in \mathbb{R}^2$, be the radioactivity distribution of a mono-energetic emitter and $\mu(\vec{x})$ be a known spatially varying attenuation medium. The attenuated Radon transform of f is

$$g(\theta, s) = \int_{-\infty}^{+\infty} f(s\vec{u}_\theta + t\vec{v}_\theta) \exp\left(-\int_t^\infty \mu(s\vec{u}_\theta + t'\vec{v}_\theta) dt'\right) dt \quad (1)$$

with $\theta \in [0, 2\pi)$ the angle of the projection, $\vec{u}_\theta = (\cos \theta, \sin \theta)^T$, $\vec{v}_\theta = (-\sin \theta, \cos \theta)^T$. We assume that we know a convex sub-region K in which the attenuation is constant ($\mu(\vec{x}) = \mu_0$, $\forall \vec{x} \in K$) and out of which the activity is zero ($f(\vec{x}) = 0$, $\forall \vec{x} \notin K$). Under these two assumptions, the exponential Radon transform can be computed from the attenuated Radon transform by a simple pointwise conversion [5]:

$$p(\theta, s) = \int_{-\infty}^{+\infty} f(s\vec{u}_\theta + t\vec{v}_\theta) e^{\mu_0 t} dt = C(\theta, s)g(\theta, s) \quad (2)$$

with

$$C(\theta, s) = \exp\left(\tau_{\theta, s}\mu_0 + \int_{\tau_{\theta, s}}^\infty \mu(s\vec{u}_\theta + t'\vec{v}_\theta) dt'\right) \quad (3)$$

where $\tau_{\theta, s}$ is the location where the photons leave the region K on their way to the detector along the lines defined by the coordinates (θ, s) . With this model, any pair of exponential projections $p(\theta_i, \cdot)$ and $p(\theta_j, \cdot)$ are consistent with each other if and only if [6]

$$P(\theta_i, \sigma_{i,j}) = P(\theta_j, \sigma_{j,i}) \quad \text{for} \quad \sigma_{i,j} = \mu_0 \tan\left(\frac{\theta_i - \theta_j}{2}\right) \quad (4)$$

where $P(\theta, \sigma) = \int_{-\infty}^\infty p(\theta, s) e^{\sigma s} ds$ is the two-sided Laplace transform of $p(\theta, \cdot)$. There is no eDCC for opposite projections, when $\theta_i - \theta_j = \pi \pmod{2\pi}$.

This result can be applied independently to each line of 2D parallel projections. We define \overline{P}_{ij} as the average value of $P(\theta_i, \sigma_{i,j})$ over the N lines of the projections

$$\overline{P}_{ij} = \frac{1}{N} \sum_{l=1}^N P_l(\theta_i, \sigma_{i,j}) \quad (5)$$

where P_l is the two-sided Laplace transform of the l -th line of the projections.

2.2 Data

A CT image of a thoracic patient was used as attenuation map. The emission map was a spherical tumor of 20 mm radius positioned approximately at the center of the liver (Figure 1). Another pair of attenuation and emission maps was defined by applying a 20 mm translation in the cranio-caudal direction to simulate a rigid motion occurring during the acquisition (the second emission map is shown in Figure 1). We used ray tracing with RTK [7] and Monte Carlo with Gate [8] to create several sets of attenuated projections. In RTK, one projector only models the attenuation effect (Equation 1) and another one models the attenuation and the PSF with parameters corresponding to a clinical dual-head SPECT system (General Electric Discovery NM/CT 670). The same system was modeled in the Monte Carlo simulation and a total of 51×10^8 140 keV emission photons of ^{99m}Tc were simulated. Several levels of scattered photons in the output projections were considered: only primary photons (no scatter), scatter correction using the double energy window [9] and no scatter correction. The projections generated with RTK were normalized against the ones obtained with Gate and Poisson noise was added. Each set of projections had 60 angles regularly sampled over 360° , each with 100×100 pixels and 4 mm isotropic spacing. In each case, one set of projections with no motion was generated and used as reference. A second set of projections was computed in which the first thirty projections correspond to the first patient position and the last thirty to the second one.

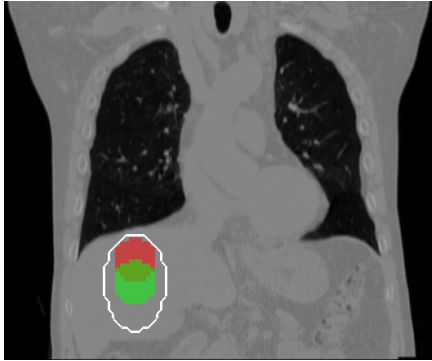


Figure 1: The two emission maps (in red and green) used to simulate SPECT projections overlaid over the attenuation map used with the green emission map. The white line corresponds to the region K used for the conversion of the attenuated projections to exponential projections.

2.3 Analysis

For each set of projections, the exponential projections were computed by choosing an elliptic region K such that it encompassed the two emission spheres while being in the liver in the two positions (Figure 1). The first attenuation map was always used for the computation of the exponential projections to mimic the clinical scenario where the CT image is acquired before the SPECT image.

Only a subset of the projection pairs was analyzed for finer analysis, those with vertical and horizontal directions, i.e. such that $\theta_1 + \theta_2 = \pi \pmod{2\pi}$ and $\theta_1 + \theta'_2 = 0 \pmod{2\pi}$ respectively (blue and red segments in Figure 2). For a pair of projections, we define the signed distance $\rho = R \vec{v}_{\theta_1} \cdot (\sin(\frac{\theta_1 + \theta_2}{2}), \cos(\frac{\theta_1 + \theta_2}{2}))^T$ with $R = 380$ mm the detector-to-isocenter distance (Figure 2). This selection allows the evaluation of the impact of the motion on the eDCCs as the 20 mm motion occurs after the first half of the acquisition (section 2.2) so the two subsets of projections taken between 0° and 174° and between 180° and 354° are consistent. Therefore, all pairs of projections with a vertical direction are not impacted by motion whereas all the ones with a horizontal direction are. Only 28 pairs in each direction were analyzed out of the $60 \times 58 = 3480$ eDCCs.

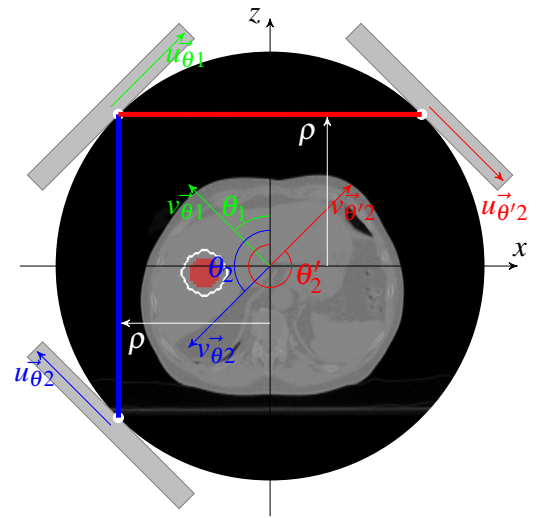


Figure 2: Selection of the pairs of projections for analyzing the eDCCs. The grey rectangles represent three detector positions and the white dots their centers. The blue and red segments symbolize two pairs of projections, vertical and horizontal respectively.

For each pair of projections, the eDCCs were computed and assessed with two metrics. The first one, was simply the average value of the absolute relative error:

$$E_{ij} = 2 * \frac{1}{N} \sum_{l=1}^N \frac{|P_l(\theta_i, \sigma_{i,j}) - P_l(\theta_j, \sigma_{j,i})|}{P_l(\theta_i, \sigma_{i,j}) + P_l(\theta_j, \sigma_{j,i})}. \quad (6)$$

Following the work of Mouchet [10], we also define a noise-aware metric which corresponds to the mean absolute difference divided by the standard deviation of the mean difference:

$$NE_{ij} = \frac{1}{N} \frac{\sum_{l=1}^N |P_l(\theta_i, \sigma_{i,j}) - P_l(\theta_j, \sigma_{j,i})|}{\sqrt{N} \sqrt{\text{Var}(\overline{P_{ij}}) + \text{Var}(\overline{P_{ji}})}}. \quad (7)$$

Using the properties of the variance of the weighted sum of random uncorrelated variables, we have

$$\text{Var}(\overline{P_{ij}}) = \frac{1}{N^2} \sum_{l=1}^N \text{Var}(P_l(\theta_i, \sigma_{i,j})). \quad (8)$$

After discretization and by applying the definition of the Laplace transform combined with the relation of equation 2 we can write

$$\text{Var}(P_l(\theta_i, \sigma_{i,j})) = \Delta s^2 \sum_{k=1}^M C_l^2(\theta_i, s_k) \text{Var}(g_l(\theta_i, s_k)) e^{2\sigma_{ij}s_k} \quad (9)$$

with Δs the pixel spacing, M the number of pixels per line and $C_l(\theta, s_k)$ and $g_l(\theta, s_k)$ the k -th pixel of the l -th line of $C(\theta, s)$ and $g(\theta, s)$. The photon noise follows a Poisson distribution so $\text{Var}(g_l(\theta_i, s_k)) = g_l(\theta_i, s_k)$ and

$$\text{Var}(\overline{P_{ij}}) = \frac{\Delta s^2}{N^2} \sum_{l=1}^N \sum_{k=1}^M C_l^2(\theta_i, s_k) g_l(\theta_i, s_k) e^{2\sigma_{ij}s_k}. \quad (10)$$

3 Results

The evolution of the metrics with the signed distance ρ characterizing a pair of projections is shown in Figure 3 for the ray tracing simulations. In the ideal case (no noise, no PSF and no motion), the relative error E_{ij} had an average value of 0.2% in the vertical and horizontal directions which indicates that the projections are consistent. With motion, the relative error in the horizontal direction became much higher (108.0% on average) and a slight increase of 2.2% in the vertical direction was observed. When modeling the PSF, the relative error of eDCCs increased even without motion between the projections. In that case, the E_{ij} value was on average 16.3% and 54.0% in the vertical and horizontal directions, respectively. With motion, the relative error also increased in the horizontal direction compared to the case without PSF. In all cases, the increase was higher when the signed distance got close to 0 mm. Additional Poisson noise in the projections produced similar results.

When assessing the eDCCs with the noise-aware metric, the inconsistency due to the PSF seemed to be mitigated. Indeed, without motion, the value of the noise-aware metric with PSF remained close to the one without PSF. In the case of motion and PSF, the value of NE_{ij} in the horizontal direction was always above the one in the vertical direction but got closer when the signed distance approached 0 mm.

Similar plots are shown in Figure 4 for the eDCCs computed from the projections obtained with Monte Carlo simulations. The main difference with the ray tracing projections with PSF and noise was the addition of scattered photons. The plot with circle markers corresponds to the simulation with primary photons only, the triangles markers to the one with DEW scatter correction and the squares to the one without scatter correction. Without motion, the relative error E_{ij} decreased with better scatter correction for pairs in the horizontal direction but the opposite was observed in the vertical direction. In the two directions, the absolute relative error was higher when the signed distance was close to 0 mm. For all levels of scattered photons, the relative error in the horizontal direction increased with the addition of the motion but the error increased with better scatter correction.

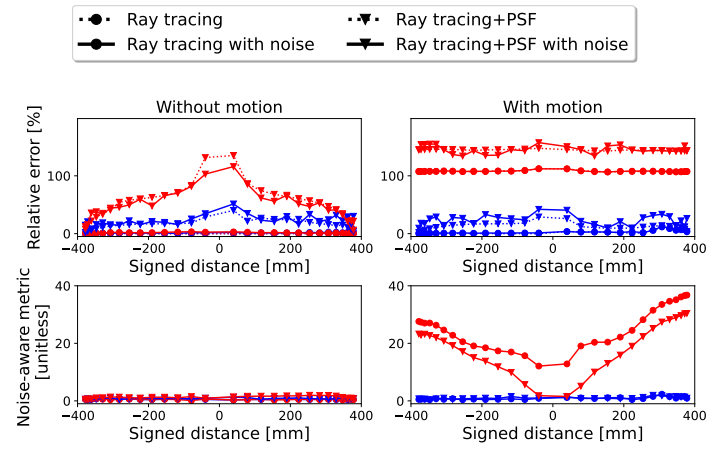


Figure 3: Relative error and noise-aware metric computed from the projections obtained with ray tracing. The blue and red lines correspond to the eDCCs computed in the vertical and horizontal directions, respectively (Figure 2). Each point is the metric of one pair of projections.

As for ray tracing simulations, the noise-aware metric seemed to reduce the error of the eDCCs. Without motion, it decreased with better scatter correction in both the horizontal and vertical directions. With motion, the value of the noise-aware metric in the horizontal direction increased and was similar for the three levels of scatter. The error was significantly higher in the horizontal direction than in the vertical direction except for the four pairs of projections where the signed distance was close to 0 mm.

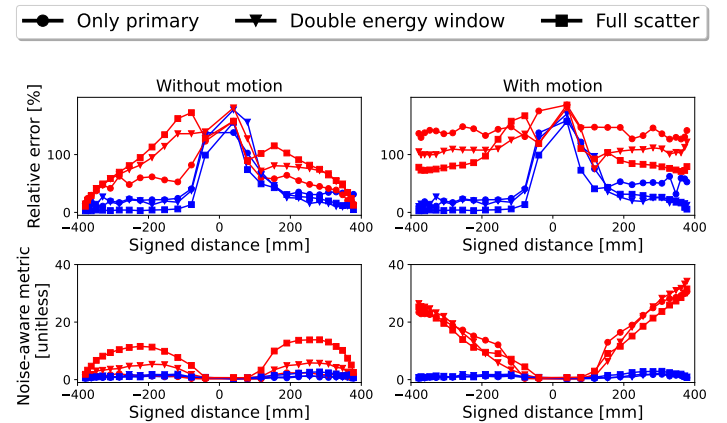


Figure 4: Relative error and noise-aware metric computed from the projections obtained with Monte Carlo simulations. The blue and red lines correspond to the eDCCs computed in the vertical and horizontal directions, respectively (Figure 2). Each point is the metric of one pair of projections.

4 Discussion

Ray-tracing and Monte Carlo simulations were used to assess the effect of noise, PSF, scatter and motion on eDCCs. They were evaluated with two metrics: the mean absolute relative error (equation 6) and a noise-aware metric (equation 7). In the closest simulations to the model of Equation 1 (ray-

tracing without modelling any physical effect), the relative error of the eDCCs was close to 0% for all the pairs of projections and therefore the projections were consistent. As noticed by Wells *et al* [4], the addition of Poisson noise slightly impacts the eDCCs.

On the other hand, the PSF appeared to have a much more detrimental effect on the eDCCs. This is due to the depth-dependence of the PSF in SPECT as the source to detector distance was not the same for the two projections in our pairs. The error increases with increasing source to detector distance difference between the projections of the pair. This is why we observed a larger inconsistency in the horizontal direction than in the vertical direction in our results. If the PSF were the same for all projections, one would expect the eDCCs to be verified. This was verified with ray tracing simulations of a centered spheroid source for which the relative error of the eDCCs was close to 0% (data not shown).

The scatter also introduced inconsistencies in the projections. At first glance, it was surprising that the relative error was not always related to the level of scatter correction. This is a side effect of the normalization as the non-normalized absolute difference $\frac{1}{N} \sum_{l=1}^N |P_l(\theta_i, \sigma_{i,j}) - P_l(\theta_j, \sigma_{j,i})|$ led to the expected result, i.e., decreasing inconsistency with increasing scatter correction (data not shown). The inconsistency is mostly due to measuring photons outside the projection of the K-region. To overcome this issue, one could mask out the SPECT projections with the forward projections of the K-region [4]. Using this approach on our data significantly mitigates the impact of scattered photons (data not shown).

The motion was the effect that introduced the largest inconsistencies. In all cases, an important increase of the error was observed in the horizontal direction when there was motion between the projections. In the vertical direction, a slight increase was noticed for the pairs of projections with a positive signed distance. These pairs correspond to the projections obtained with the shifted emission map in both projections but the non-shifted attenuation map was used for the computation of the exponential projections (Equation 2) which introduced small inconsistencies. The error of most pairs of projections was still much higher in the horizontal direction than in the vertical one making the eDCCs a promising solution to detect patient motion during SPECT acquisitions. In all cases, the absolute relative error was higher when the signed distance got close to 0 mm i.e. when the projections of the pair were close to be 180° apart. When taking the Laplace transform, the exponential projections are multiplied by $\exp(\sigma_{ij}s)$ and $\lim_{\theta_i - \theta_j \rightarrow \pi} \sigma_{ij} = +\infty$ so for projections close to be 180° apart, small inconsistencies could be highly magnified. By using the noise-aware metric that takes into account the variance of the measurement, we managed to reduce this effect. This metric is also more robust to the inconsistencies introduced by the PSF and the scatter and therefore more suitable for motion detection or for applying the method to real acquisitions.

5 Conclusion

eDCCs were evaluated on simulated datasets with increasing levels of realism. The PSF, the scatter and the movement were source of inconsistencies in the projections. We introduced a noise-aware metric which seems to be more robust to the PSF and scatter effects and which might be a promising way to detect patient motion.

Acknowledgement

This work was supported by grant ANR-21-CE45-0026 (SPECT-Motion-eDCC) from the French National Research Agency (ANR) and was performed within the framework of the SIRIC LYriCAN INCa-INSERM-DGOS-12563 and the LABEX PRIMES (ANR-11-LABX-0063) of Université de Lyon, within the program "Investissements d'Avenir" (ANR-11-IDEX-0007) operated by the ANR.

References

- [1] D. Zhang, B.-H. Yang, N. Y. Wu, et al. "Respiratory Average CT for Attenuation Correction in Myocardial Perfusion SPECT/CT". *Annals of Nuclear Medicine* 31.2 (Feb. 2017), pp. 172–180. DOI: [10.1007/s12149-016-1144-1](https://doi.org/10.1007/s12149-016-1144-1).
- [2] C. R. R. N. Hunter, R. Klein, A. M. Alessio, et al. "Patient Body Motion Correction for Dynamic Cardiac PET-CT by Attenuation-Emission Alignment According to Projection Consistency Conditions". *Medical Physics* 46.4 (2019), pp. 1697–1706. DOI: [10.1002/mp.13419](https://doi.org/10.1002/mp.13419).
- [3] A. Welch, R. Clack, F. Natterer, et al. "Toward Accurate Attenuation Correction in SPECT without Transmission Measurements". *IEEE transactions on medical imaging* 16.5 (Oct. 1997), pp. 532–541. DOI: [10.1109/42.640743](https://doi.org/10.1109/42.640743).
- [4] R. G. Wells and R. Clackdoyle. "Feasibility of Attenuation Map Alignment in Pinhole Cardiac SPECT Using Exponential Data Consistency Conditions". *Medical Physics* 48.9 (Sept. 2021), pp. 4955–4965. DOI: [10.1002/mp.15058](https://doi.org/10.1002/mp.15058).
- [5] F. Natterer. *The Mathematics of Computerized Tomography*. SIAM, 1986.
- [6] V. Aguilar, L. Ehrenpreis, and P. Kuchment. "Range Conditions for the Exponential Radon Transform". *Journal d'Analyse Mathématique* 68.1 (Dec. 1996), pp. 1–13. DOI: [10.1007/BF02790201](https://doi.org/10.1007/BF02790201).
- [7] S. Rit, M. Vila Oliva, S. Brousmiche, et al. "The Reconstruction Toolkit (RTK), an Open-Source Cone-Beam CT Reconstruction Toolkit Based on the Insight Toolkit (ITK)". *Journal of Physics: Conference Series* 489 (Mar. 2014), p. 012079. DOI: [10.1088/1742-6596/489/1/012079](https://doi.org/10.1088/1742-6596/489/1/012079).
- [8] S. Jan, D. Benoit, E. Becheva, et al. "GATE V6: A Major Enhancement of the GATE Simulation Platform Enabling Modelling of CT and Radiotherapy". *Physics in Medicine and Biology* 56.4 (Feb. 2011), pp. 881–901. DOI: [10.1088/0031-9155/56/4/001](https://doi.org/10.1088/0031-9155/56/4/001).
- [9] R. J. Jaszczak, K. L. Greer, C. E. Floyd, et al. "Improved SPECT Quantification Using Compensation for Scattered Photons". *Journal of Nuclear Medicine* 25.8 (Aug. 1984), pp. 893–900.
- [10] M. Mouchet, S. Rit, J. Lessaint, et al. "Variance of Cone-Beam Pair-Wise Consistency Conditions in Helical CT". *2022 IEEE Nuclear Science Symposium and Medical Imaging Conference (NSS/MIC)*. In Press. Nov. 2022.